Check for updates

Enhanced photocatalytic activity of BiOI under visible light irradiation by the modification of MoS₂

Yuzhen Bu, Junli Xu, [ID]* Yawen Li, Qian Liu and Xia Zhang [ID]

3D hierarchical BiOI nanostructures modified with MoS₂ were successfully fabricated through a simple solvent thermal process. The prepared heterostructured BiOI–MoS₂ nanocomposite exhibited excellent photocatalytic performance in the degradation of methyl orange under visible light irradiation. The photocatalytic activity of BiOI–MoS₂ increases with the increase of MoS₂ content first, then it decreases when MoS₂ content is over 0.5 wt%. The degradation efficiency of methyl orange could achieve 95% within 90 min in the presence of BiOI–0.5 wt% MoS₂, which is about two times higher than that of pristine BiOI nanostructures. The obviously improved photocatalytic performance of BiOI–MoS₂ could be mainly attributed to the significantly enhanced separation efficiency of photogenerated charge carriers. However, too much MoS₂ loading on the surface of BiOI will prevent light from reaching surface of BiOI and limit the efficiency of charge separation. Based on active species trapping experiments, holes (h⁺) were proved to be the main reactive species in the prepared BiOI–MoS₂ system.

1 Introduction

Bismuth oxyhalides (BiOX), in which X is a halogen element, is a layered compound having an open, layered crystal structure consisting of positive [Bi₂O₂] layers sandwiched between two slabs of negative halogen ions.[1,2] These unique layered structures make BiOX exhibit good adsorption properties and excellent photocatalytic activities in waste water and indoor air purification.[3–5] Among the BiOX family, BiOI is found to be a promising photocatalyst for the removal of organic pollutants under visible light irradiation since BiOI possesses the smallest band gap (E_g = 1.73–1.92 eV) and strong absorption.[6–8] However, pure BiOI is always poor in photocatalytic activity because of the rapid recombination of photoinduced electron–hole pairs.[9,10] It is important to facilitate the separation of electron–hole pairs and thus improve the photocatalytic activities of BiOI. Development of a highly efficient visible light response of BiOI based catalysts to meet the requirement of practical application still remains a challenge.

It is well known that semiconductor combination is an efficient way for the separation of photoinduced carries, and thus raises the photocatalytic efficiency since a heterojunction structure may be formed between different semiconductors.[11,12] This heterostructure composite photocatalyst results in an efficient charge separation at the interface. Several heterostructure based on BiOI have been reported which showed higher photocatalytic activity than pure BiOI, such as BiOI/WO₃,[13,14] BiOI/AgI,[15–17] BiOI/Ag,[18–20] BiOI/Ag/AgI,[21–23]

AgI/BiOI–Bi₂O₃,[24] BiOI/Bi₂WO₆,[25] BiOI/Ag₃PO₄,[26] BiOI/Bi₂MoO₆,[27] BiOI/ZnSn(OH)₆,[28] BiOI/BiOBr.[29]

MoS₂ has a sandwich interlayer structure composed of three stacked atom layers (S–Mo–S) which are bonded together by weak van der Waals forces.[30] The monolayer MoS₂ has been successfully synthesized, and get particular attention in photovoltaic application due to its distinctive electronic, optical, large surface area and catalytically active sites.[31–33]

In view of the fact that MoS₂ and BiOI are similar in structure, it is envisaged that a BiOI/MoS₂ composite can have the merits of MoS₂ and BiOI, consequently showing high photocatalytic activity under visible light. However, seldom research has been reported on BiOI/MoS₂ composite photocatalytic performance until now. Recently, 2D structure BiOI/MoS₂ (ref. 34) and 3D hierarchical BiOI/MoS₂/AgI[35] were reported which exhibited good photocatalytic activity towards rhodamine B degradation. The degradation efficiencies of RhB after 50 min were 20%, 40% and 96% by 3D hierarchical BiOI, BiOI/AgI and MoS₂/BiOI/AgI under simulated solar irradiation, respectively. However, the photocatalytic activity of 3D hierarchical BiOI/MoS₂ under visible light irradiation has not been reported yet. Therefore, 3D hierarchical BiOI/MoS₂ composite was fabricated by a simple solvent thermal process in this work, and the results show that the as-prepared BiOI/MoS₂ composites exhibited an excellent photocatalytic activity for the degradation of methyl orange (MO) in visible light irradiation. The possible photocatalytic mechanism of BiOI/MoS₂ heterostructure to MO degradation is proposed by adding radical scavengers in the photocatalytic system.

College of Science, Northeastern University, Shenyang, 110004, China. E-mail: jlxu@mail.neu.edu.cn; Fax: +86-24-83684533; Tel: +86-24-83684533

2 Experimental methods

2.1 Synthesis of MoS₂, BiOI and BiOI–MoS₂ composites

All chemical reagents were of analytical grade and used without further purification in this study. For the preparation of MoS_2, 5 mmol Na_2MoO_4 and 20 mmol $CS(NH_2)_2$ were dissolved in deionized water with vigorous stirring for 1 h at room temperature. Then, the mixture was transferred into a 100 ml Teflon-lined stainless-steel autoclave. The autoclave was kept at 483 K for 24 h. The sample was obtained by filtration, washed with deionized water and absolute ethanol many times, and then dispersed into absolute ethanol and dried for 12 h at 323 K.

BiOI/MoS_2 composite were synthesized by an ethylene glycol (EG)-assisted solvothermal method. In a typical synthesis procedure, 2 mmol $Bi(NO_3)_3 \cdot 5H_2O$ and 2 mmol KI was dissolved in 15 ml ethylene glycol under ultrasonication for 20 min respectively first. Then, the two solutions were mixed and some MoS_2 was added to the mixture. The mixture was under vigorous stirring for 15 min, then it was transferred into a 100 ml Teflon-lined stainless-steel autoclave. The autoclave was kept at 433 K for 12 h. The resultant precipitates were collected, repeatedly washed with deionized water and ethanol, and dried for 12 h at 333 K. BiOI/MoS_2 composites were named as BiOI- (wt% of MoS_2) MoS_2. For comparison, BiOI was also fabricated as the same method without the presence of MoS_2.

2.2 Characterization

The morphologies of the prepared BiOI, MoS_2 and BiOI–(0.5%) MoS_2 samples were characterized by a PANalytical B.V. MPDDY2094 X-ray diffractometer (XRD) with Cu Kα radiation ($\lambda = 1.5406$ Å). Scanning electron microscopy (SEM) pictures and quantitative standard microanalyses were obtained using an energy dispersive X-ray analysis (EDS) with a Zeiss ultra plus FESEM apparatus. UV-vis diffuse reflectance spectrum (DRS) was recorded on a Perkin Elmer Lambda 35 UV-vis spectrophotometer with $BaSO_4$ as a reference, and the scanned range being 200–800 nm against barium sulfate standard. N_2 adsorption–desorption isotherm was conducted on a Micromeritics ASAP-2020-HD88 volumetric gas sorption apparatus using 99.999% pure N_2.

The photoluminescence (PL) measurements were performed on a Hitachi F7000 Fluorescence Spectrophotometer with an excitation wavelength of 325 nm at room temperature. The photocurrents were performed in 0.5 mol l^{-1} Na_2SO_4 solution using an electrochemistry workstation (CHI 660, China) with a three-electrode system. The obtained sample was served as the working electrode (1 mg of the as-prepared sample was dispersed in 0.2 ml of ethanol and 0.2 ml of ethanol mixture to produce a suspension, which was then dip-coated onto an ITO glass electrode). A platinum plate and a saturated Ag/AgCl were used as the counter electrode and reference electrode, respectively. A 300 W Xe lamp with main emission wavelength 420 nm in the range of 420–780 nm along with a power of 80 mW cm^{-2} was utilized as the photosource.

2.3 Photocatalytic activity tests

The photocatalytic activity tests of the obtained samples were investigated by evaluating in terms of the degradation of methyl orange (MO) solution under the simulated sunlight irradiation. The photochemical reactor contains 40 mg catalysts and 5.0×10^{-5} mol l^{-1} of 100 ml MO. A 300 W Xe lamp with main emission wavelength 420 nm in the range of 420–780 nm along with a power of 20 mW cm^{-2} (Beijing Science and Technology Co., Ltd. Park Philae), was set inside a cylindrical reactor, and surrounded by a circulating water jacket to cool the lamp and minimize infrared radiation. The methyl orange aqueous solutions with the added catalysts were kept in the dark for some minutes to establish the adsorption equilibrium of the methyl orange for the catalyst before exposure to the simulated sunlight. After exposure to the radiation for different intervals, the UV-vis spectrophotometer (TU-1900, Beijing Purkinje General Instrument Co., Ltd.) was used to determine the solution concentration of methyl orange. The absorbance accuracy is ±0.002 Abs (0–0.5 Abs), and ±0.004 Abs (0.5–1.0 Abs).

3 Results and discussion

3.1 Structure and morphology

Fig. 1 shows the XRD patterns of prepared MoS_2, BiOI and BiOI–MoS_2 samples. The diffraction peaks of 14.43° (002), 33.61° (100), 39.88° (103), 58.87° (110) can be indexed to MoS_2 (JCPDS card no. 01-087-2416), while 24.57° (101), 29.55° (102), 32.13° (110), 36.56° (103), 45.59° (104), 50.39° (114), 55.19° (212), 66.44° (214), 75.48° (310) diffraction peaks are belong to tetragonal phase BiOI (JCPDS card no. 00-010-0445). No peaks of other impurities are observed in the diffraction peaks of the as prepared BiOI and MoS_2, indicating that the high purity and single phase of the prepared BiOI and MoS_2 products. Moreover, diffraction peaks of MoS_2 can be found hardly because of its relatively low content in the prepared BiOI–MoS_2 samples.

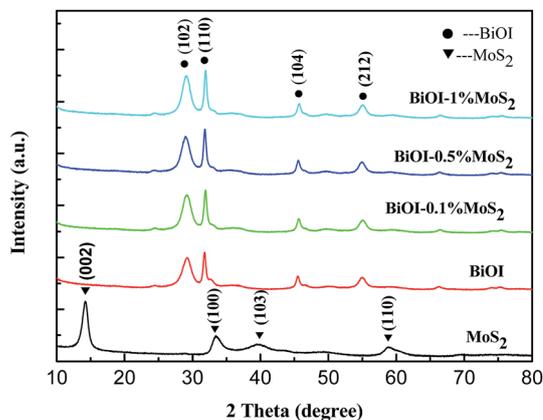FESEM images of the MoS_2, BiOI and BiOI–0.5% MoS_2 samples are shown in Fig. 2.

Fig. 1 X-ray diffraction patterns of prepared MoS_2, BiOI and BiOI–MoS_2 samples.
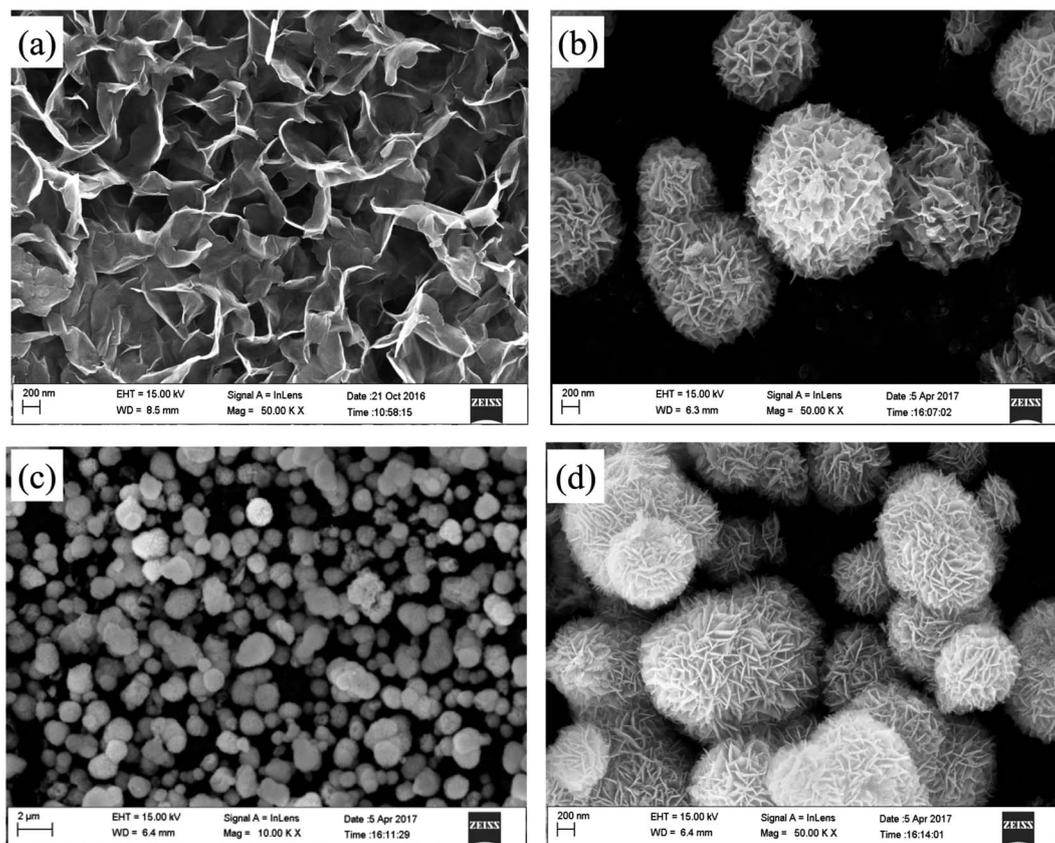
Fig. 2 FESEM images of MoS$_2$ (a), BiOI (b) and BiOI−0.5% MoS$_2$ (c and d).

As shown in Fig. 2(a), the synthesized MoS$_2$ sample structure is composed of curled and interlaced nanosheets, while BiOI and BiOI–0.5% MoS$_2$ samples exhibit a similar 3D flower-like hierarchical spherical structure. The flower-like structures have wide size distribution and diameters ranging from approximately 600 nm to 1.5 μm. Moreover, these microspheres are not completely isolated from each other, but often coupled together. Compare with pristine BiOI, BiOI–0.5% MoS$_2$ has smaller spherical size. Close examination of the morphology of reveals that the hierarchical microsphere consisting of loosely stacked nanoplates with an average slide length of about 200 nm. This specific hierarchical nanostructures make the samples have an obvious high surface-to-volume ratio, which is favourable for pollutant molecules transportation and light injection.[36,37]

3.2 Optical properties

The optical properties of the samples were investigated by ultraviolet-visible diffuse reflectance spectra and depicted in Fig. 3(a), and the curves of $(\alpha h\nu)^{1/2}$ *versus* $h\nu$ derived from the UV-visible spectra are presented in Fig. 3(b). As shown in Fig. 3(b), the loading of MoS$_2$ can significantly affect the band gap energy compare to pristine BiOI, and the extent of band gap energy greatly depends upon the loading level. The pristine BiOI and MoS$_2$ exhibit a band gap energy of 1.87 eV and 1.71 eV respectively, which is close to the values reported in

other literatures.[1,38,39] Moreover, BiOI–MoS$_2$ composites exhibit larger band gap energy than that of BiOI, as BiOI–MoS$_2$ composites exhibit a band gap energy of about 2.25 eV (BiOI–0.1% MoS$_2$), 2.30 eV (BiOI–0.5% MoS$_2$) and 2.25 eV (BiOI–1% MoS$_2$) respectively. Although the addition of MoS$_2$ in BiOI enlarged the band gap of BiOI, the absorbance of BiOI–MoS$_2$ samples are much stronger than that of pristine BiOI in the visible region, which allows the BiOI–MoS$_2$ catalysts to utilize more visible light during photocatalytic degradation and is expected to enhance the photocatalytic behavior.[40]

3.3 Adsorption–desorption analysis

The N$_2$ adsorption–desorption isotherms of the pristine BiOI and BiOI–0.5% MoS$_2$ samples are shown in Fig. 4. Both of the isotherms exhibit a typical IV isotherm with a hysteresis loop, suggesting their mesoporous features, which is also confirmed by the corresponding pore size distribution curve (inset in Fig. 4). As shown in Table 1, the BET surface areas were calculated to be 52.87 and 48.81 m^2 g^{-1} for pristine BiOI and BiOI–0.5% MoS$_2$ respectively. In addition, the average mesoporous diameter of BiOI–0.5% MoS$_2$ is larger than that of pristine BiOI. The BET surface area values did not have obvious difference, which indicates that the BET surface area has little effect on the photocatalytic performance of obtained BiOI and BiOI–0.5% MoS$_2$ samples.
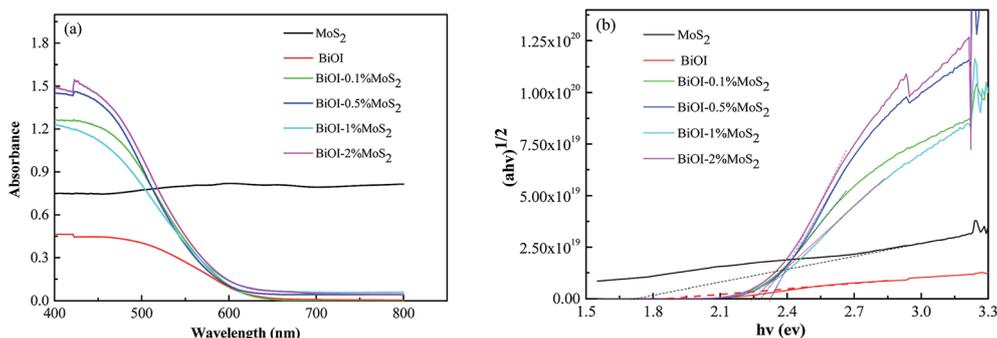
Fig. 3 (a) UV-Vis diffused reflectance spectra of pristine MoS_2, BiOI and BiOI–MoS_2 samples; (b) the plots of transformed Kubelka–Munk function *versus* the energy of light.
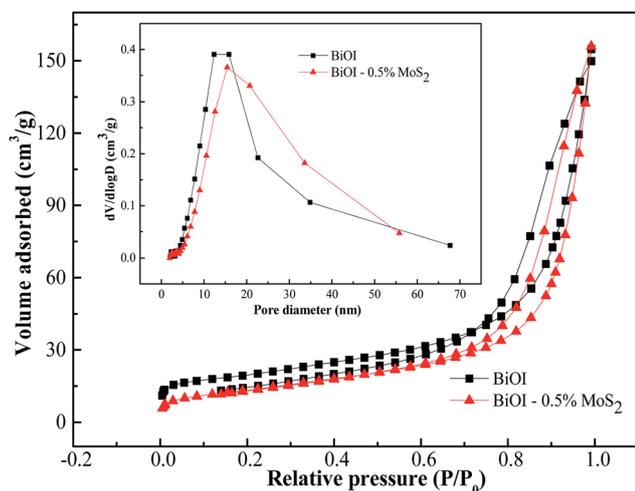

Fig. 4 N_2 adsorption and desorption isotherms and the corresponding pore-size distribution (inset) for the BiOI and BiOi–0.5% MoS_2 samples.

Table 1 Textural features of BiOI and BiOI–0.5% MoS_2 samples

Semiconductor	BET surface area (m^2 g^{-1})	Pore volume (cm^3 g^{-1})	Average pore diameter (nm)
BiOI	52.87	0.23	13.60
BiOI–0.5% MoS_2	48.81	0.24	16.57

3.4 FTIR analysis

The FTIR spectra of pure BiOI and BiOI–MoS_2 hybrids are shown in Fig. 5. The peak at around 520 cm^{-1} is corresponded to the stretching vibration of the Bi–O.[41] Compared with pure BiOI, the stretching vibration of Bi–O in BiOI–MoS_2 samples shift to higher frequency region slightly, indicating that there are strong interaction between BiOI and MoS_2.[34,42] The strong interaction between BiOI and MoS_2 may be beneficial to the separation of photo-induced charge carriers. In addition, the peak at around 1620 cm^{-1} is ascribed to the bending vibration absorption of free water molecules, and the broad peak at around 3420 cm^{-1} is related to the stretching vibrations of O–H,[43,44] which could serve as anchor to the contaminant molecules.

3.5 Photocatalytic performance

The degradations of methyl orange dye by BiOI–MoS_2 samples under visible light irradiation are shown in Fig. 6(a). Error bars in Fig. 6 represent SDs calculated from three parallel experiments. About 50% MO was photodegraded by pristine BiOI, and the introduction of MoS_2 into BiOI can enhance the degradation efficiency. BiOI–0.5% MoS_2 sample exhibits the best excellent photocatalytic activity towards MO, and the photodegradation rate could reach 95% under 90 min of visible light irradiation. Compared to other reported BiOI composites, the prepared BiOI–MoS_2 composites shows higher photodegradation properties to MO as shown in Table 2.

The stability is one of the important considerations for the application of a photocatalyst. Recycling experiments on the photocatalytic degradation of methyl orange dye were carried out as shown in Fig. 6(b). The degradation rate is about 80% for the second and third cycles, while it could maintain at 60% after four successive cycles. Fig. 7 shows the microstructure of BiOI–0.5% MoS_2 which had gone through four cycles photocatalysis tests. Compared with the microstructure of BiOI–0.5% MoS_2 before cycles (Fig. 2(c) and (d)), there are more small particles on the surface of spherical BiOI, which indicates the disaggregation of the sponge structure of BiOI. The decrease of the photocatalytic activity may be due to the disaggregation of the sponge structure of BiOI.
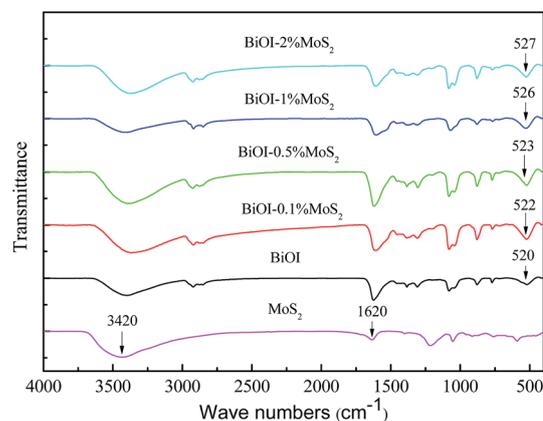

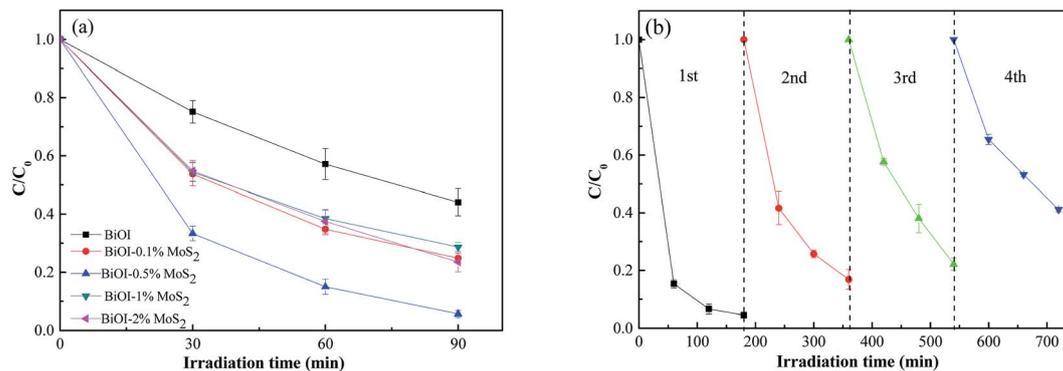**Fig. 5** FTIR spectra of BiOI, MoS_2 and BiOI–MoS_2 samples.

Fig. 6 Degradation properties of MO by BiOI–MoS$_2$ samples under visible light irradiation. (a) The relationship between degradation efficiency of MO and irradiation time. (b) Recycling property of BiOI–0.5% MoS$_2$ in the degradation of MO.

Table 2 Photodegradation properties of some reported BiOI based composites to MO solution under visible light irradiation

Photocatalyst	Photodegradation conditions (photocatalyst mass, MO solution concentration, MO solution volume, photodegradation time)	Photodegradation rate	Reference number
BiOI–1 wt% WO$_3$	100 mg, 10 mg l^{-1}, 150 ml, 100 min	70%	14
BiOI–20 wt% AgI	100 mg, 20 mg l^{-1}, 100 ml, 180 min	90%	15
BiOI–Ag	100 mg, 10 mg l^{-1}, 50 ml, 120 min	90%	18
BiOI–0.6 wt% Ag	50 mg, 10 mg l^{-1}, 50 ml, 240 min	80%	20
BiOI–Ag–AgI (6 wt% Ag–AgI)	100 mg, 10 mg l^{-1}, 50 ml, 180 min	93%	22
BiOI–Ag$_3$PO$_4$ (1 : 2 mol ratio)	50 mg, 3.2 mg l^{-1}, 50 ml, 100 min	70%	26
BiOI–0.5 wt% MoS$_2$	40 mg, 16 mg l^{-1}, 100 ml, 90 min	95%	This report

Photoluminescence (PL) spectrum and photocurrent generation are effective techniques to evaluate the efficiency of charge carrier trapping, transfer and separation in semiconductor materials and surface defects of samples. Fig. 8(a) shows the room temperature PL spectra of prepared BiOI and BiOI–MoS$_2$ composites with an excitation wavelength of 325 nm. There are three intense emission peaks centered around 370 nm, 590 nm and 620 nm. The BiOI–0.5% MoS$_2$ exhibited the lowest peak intensity, while BiOI exhibited the highest peak intensity. This result implies BiOI–0.5% MoS$_2$ has the lowest rate of

recombination of photogenerated charge carriers, while BiOI has the highest rate of recombination of photogenerated charge carriers.

Fig. 8(b) showed the photocurrent response of BiOI, MoS$_2$ and BiOI–0.5% MoS$_2$ with illumination of visible light. The rapid increase photocurrent response from a light-off to light-on state was mainly due to the fast separation and transfer of the photogenerated electrons on the surface of the working electrode. As shown in Fig. 8(b), the photocurrent density generated by BiOI–0.5% MoS$_2$ was much higher than that by
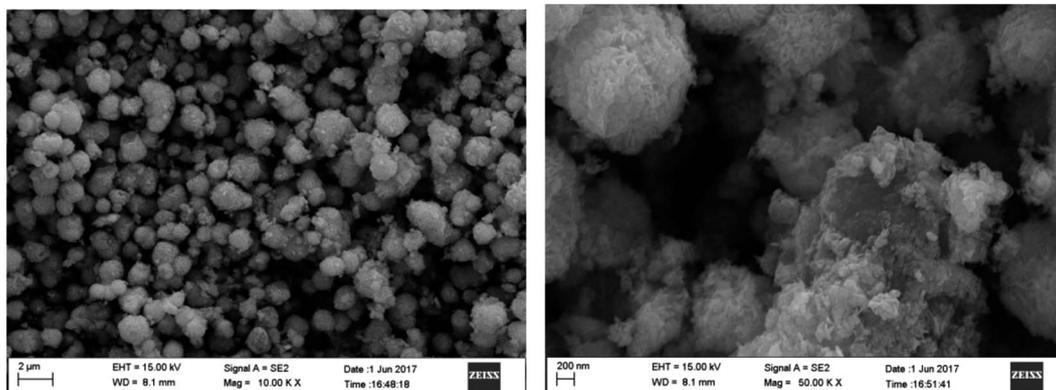

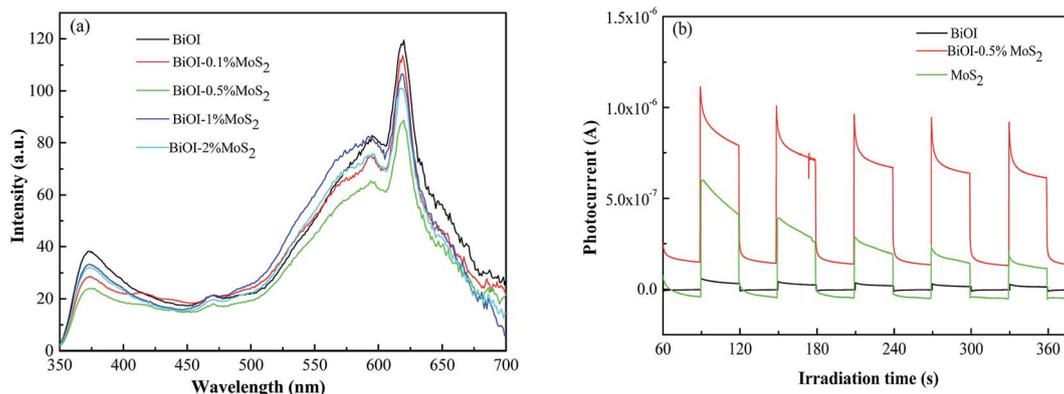**Fig. 7** FESEM images of BiOI–0.5% MoS$_2$ after four photocatalysis cycles.

Fig. 8 (a) Photoluminescence spectra of BiOI and BiOI–MoS$_2$ composites; (b) transient photocurrent response of BiOI, MoS$_2$ and BiOI–0.5% MoS$_2$ under visible light irradiation.

BiOI, which indicate that BiOI–0.5% MoS$_2$ has more efficiency separation rate of photogenerated carriers than BiOI. This result is consistent with the results of PL, and it could be speculated that the separation of photogenerated carriers may be one of the reasons for the highest photocatalytic performance of BiOI–0.5% MoS$_2$ on MO degradation.

Moreover, the energy of conduction band edge (E_{CB}) and the energy of valence band edge (E_{VB}) can be calculated by using the following equations:[45]

$$E_{CB} = -\chi + 0.5E_g \qquad (1)$$

and

$$E_{VB} = -\chi - 0.5E_g \qquad (2)$$

where, χ is the absolute electronegativity of the semiconductor, and E_g is the band gap energy of the semiconductor. The absolute electronegativity of BiOI and MoS$_2$ is 5.99 eV (ref. 8) and 5.32 eV (ref. 45) respectively. As the pristine BiOI and MoS$_2$ exhibit a band gap energy of 1.87 eV and 1.71 eV respectively as

shown in Fig. 3(b), the calculated E_{CB} and E_{VB} of BiOI is about −5.05 eV and −6.93 eV, while it is −4.46 eV and −6.18 eV for MoS$_2$ respectively. Therefore, it is thermodynamically favorable for the direct electron transfer from the conduction band of MoS$_2$ to the conduction band of BiOI, while the holes transfer from the valance band of BiOI to the valance band of MoS$_2$ as shown in Fig. 9.

3.6 Photocatalytic mechanism

To survey the photocatalytic disinfection mechanism, active species trapping experiments were conducted and the results are shown in Fig. 10. Error bars in Fig. 10 represent SDs calculated from three parallel experiments. Ammonium oxalate and isopropanol were chose as h$^+$ scavengers and OH scavengers respectively. As shown in Fig. 10, comparing with the photodegradation efficiency without scavenger, the photodegradation efficiency is decreased obviously when ammonium oxalate was added into the MO solution. However, it is only a little decreased when isopropanol was added into the MO solution. This result indicates that h$^+$ was the main reactive
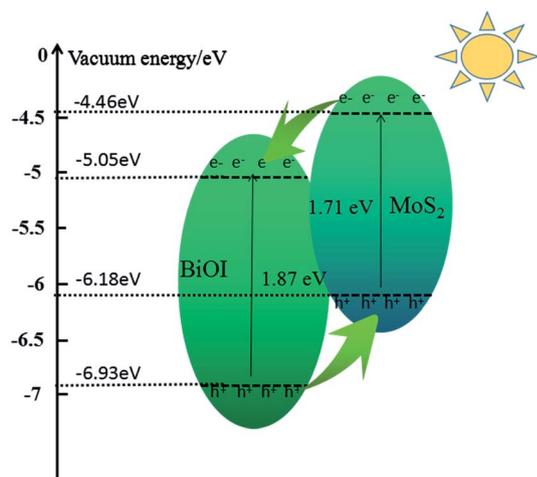

Fig. 9 Schematic diagram illustrating the principle of photo-induced charge transfer in BiOI–MoS$_2$ semiconductor.
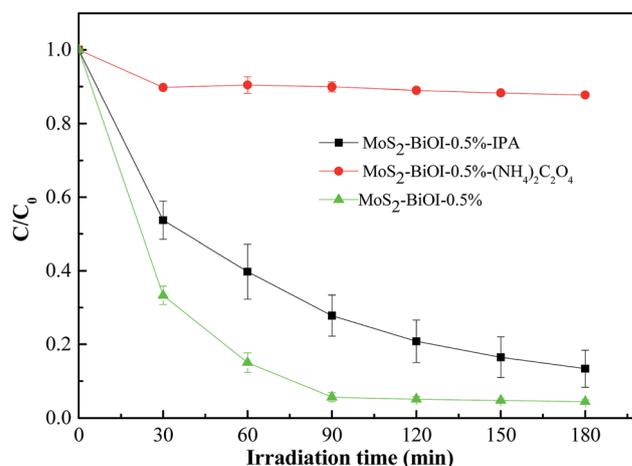

Fig. 10 Scavenger effects on the degradation of MO solution under visible light irradiation.

species in the photodegradation of MO for the prepared BiOI–MoS$_2$ samples under visible light irradiation.

3.7 Discussion on the effects of MoS$_2$ on the photocatalytic activity

From Fig. 6, it is deduced that the photocatalytic activity of BiOI increased with the loading of MoS$_2$ on BiOI. The photocatalytic activity of BiOI–MoS$_2$ increases with the increase of MoS$_2$ contents first, then it decreases when MoS$_2$ content is over 0.5 wt%. This can be attributed to two main reasons. First, it is thermodynamically favorable for the direct electron transfer from the conduction band of MoS$_2$ to the conduction band of BiOI, while the holes transfer from the valance band of BiOI to the valance band of MoS$_2$ as shown in Fig. 9. Thus, the modification of MoS$_2$ on BiOI can accelerate the division and restrain the recombination of photogenerated electron–hole pairs, resulting in the improved photocatalytic activity. Second, too much MoS$_2$ loading on the surface of BiOI will prevent light from reaching surface of BiOI, and thus reduce the generation of electrons and holes. In addition, too much MoS$_2$ loading will also limit the efficiency of charge separation, which is confirmed by the photoluminescence spectra of pure BiOI and BiOI–MoS$_2$ composites as shown in Fig. 8(a).

4   Conclusions

3D hierarchical BiOI modified by MoS$_2$ with excellent photo-catalytic performance in the degradation of methyl orange under visible light irradiation were successfully fabricated through a simple solvent thermal process. The photocatalytic activity of BiOI–MoS$_2$ for the degradation of methyl orange increases with the increase of MoS$_2$ contents first, then it decreases when MoS$_2$ content is over 0.5 wt%. The degradation efficiency of methyl orange for BiOI–0.5% MoS$_2$ is about two times higher than that of bare BiOI nanostructures. The enhanced photocatalytic activities could be attributed to higher separation efficiency of photogenerated charge carriers. However, radicals and holes trapping experiments showed that h$^+$ dominates the photodegradation process of MO.

Conflicts of interest

There are no conflicts to declare.

Acknowledgements

References

1 X. Zhang, Z. H. Ai, F. L. Jia and L. Z. Zhang, Generalized one-pot synthesis, characterization, and photocatalytic activity of hierarchical BiOX (X = Cl, Br, I) nanoplate microspheres, *J. Phys. Chem. C*, 2008, **112**(3), 747–753.

2 X. Y. Qin, H. F. Cheng, W. J. Wang, B. B. Huang, X. Y. Zhang and Y. Dai, Three dimensional BiOX (X = Cl, Br and I) hierarchical architectures: facile ionic liquid-assisted solvothermal synthesis and photocatalysis towards organic dye degradation, *Mater. Lett.*, 2013, **100**(6), 285–288.

3 K. L. Zhang, C. M. Liu, F. Q. Huang, C. Zheng and W. D. Wang, Study of the electronic structure and photocatalytic activity of the BiOCl photocatalyst, *Appl. Catal., B*, 2006, **68**(3–4), 125–129.

4 W. D. Wang, F. Q. Huang, X. P. Lin and J. H. Yang, Visible-light-responsive photocatalysts xBiOBr-(1-x)BiOI, *Catal. Commun.*, 2008, **9**(1), 8–12.

5 J. Cao, B. Y. Xu, B. D. Luo, H. L. Lin and S. F. Chen, Novel BiOI/BiOBr heterojunction photocatalysts with enhanced visible light photocatalytic properties, *Catal. Commun.*, 2011, **13**(1), 63–68.

6 X. F. Chang, J. Huang, C. Cheng, Q. Sui, W. Sha, G. B. Ji, S. B. Deng and G. Yu, BiOX (X = Cl, Br, I) photocatalysts prepared using NaBiO$_3$, as the Bi source: characterization and catalytic performance, *Catal. Commun.*, 2010, **11**(5), 460–464.

7 W. D. Wang, F. Q. Huang and X. Q. Lin, xBiOI-(1-x)BiOCl as efficient visible-light-driven photocatalysts, *Scr. Mater.*, 2007, **56**(8), 669–672.

8 Y. G. Li, J. S. Wang, H. C. Yao, L. Y. Dang and Z. J. Li, Efficient decomposition of organic compounds and reaction mechanism with BiOI photocatalyst under visible light irradiation, *J. Mol. Catal. A: Chem.*, 2011, **334**(1–2), 116–122.

9 Y. F. Chen, J. H. Fang, S. Y. Lu, Y. Wu, D. Z. Chen, L. Y. Huang, W. C. Xu, X. M. Zhu and Z. Q. Fang, Fabrication characterization and photocatalytic properties of Ag/AgI/BiOI heteronanostructures supported on rectorite via a cation-exchange method, *Mater. Res. Bull.*, 2015, **64**(64), 97–105.

10 Y. Q. Lei, G. H. Wang, S. Y. Song, W. Q. Fan, M. Pang and J. K. Tang, Room temperature, template-free synthesis of BiOI hierarchical structures: visible-light photocatalytic and electrochemical hydrogen storage properties, *Dalton Trans.*, 2010, **39**(13), 3273–3278.

11 H. J. Li, Y. Zhou, W. G. Tu, J. H. Ye and Z. G. Zou, State-of-the-Art Progress in Diverse Heterostructured Photocatalysts toward Promoting Photocatalytic Performance, *Adv. Funct. Mater.*, 2015, **25**(7), 998–1013.

12 S. J. A. Moniz, S. A. Shevlin, D. J. Martin, Z. X. Guo and J. W. Tang, Visible-light driven heterojunction photocatalysts for water splitting-a critical review, *Energy Environ. Sci.*, 2015, **8**(3), 731–759.

13 Y. Feng, C. B. Liu, H. N. Che, J. B. Chen, K. Huang, C. Y. Huang and W. D. Shi, The highly improved visible light photocatalytic activity of BiOI through fabricating a novel p–n heterojunction BiOI/WO$_3$ nanocomposite, *CrystEngComm*, 2016, **18**(10), 1790–1799.

14 J. Luo, X. S. Zhou, L. Ma and X. Y. Xu, Enhanced visible-light-driven photocatalytic activity of WO$_3$/BiOI heterojunction photocatalysts, *J. Mol. Catal. A: Chem.*, 2015, **410**, 168–176.

15 H. F. Cheng, B. B. Huang, Y. Dai, X. Y. Qin and X. Y. Zhang, One-step synthesis of the nanostructured AgI/BiOI

composites with highly enhanced visible-light photocatalytic performances, *Langmuir*, 2010, **26**(9), 6618–6624.

16 J. M. Gong, F. Tian, D. H. Peng, A. M. Li and L. Z. Zhang, A highly sensitive photoelectrochemical detection of perfluorooctanic acid with molecularly imprinted polymer-functionalized nanoarchitectured hybrid of AgI-BiOI composite, *Biosens. Bioelectron.*, 2015, **73**, 256–263.

17 J. L. Liang, C. Shan, X. Zhang and M. P. Tong, Bactericidal mechanism of BiOI-AgI under visible light irradiation, *Chem. Eng. J.*, 2015, **279**, 277–285.

18 C. C. Zhou, J. Cao, H. L. Lin, B. Y. Xu, B. B. Huang and S. F. Chen, Controllable synthesis and photocatalytic activity of Ag/BiOI based on the morphology effect of BiOI substrate, *Surf. Coat. Technol.*, 2015, **272**, 213–220.

19 L. F. Zhu, C. He, Y. L. Huang, Z. H. Chen, D. H. Xia, M. H. Su, Y. Xiong, S. Y. Li and D. Shu, Enhanced photocatalytic disinfection of E. Coli 8099 using Ag/BiOI composite under visible light irradiation, *Sep. Purif. Technol.*, 2012, **91**(91), 59–66.

20 H. Liu, W. R. Cao, Y. Su, Y. Wang and X. H. Wang, Synthesis characterization and photocatalytic performance of novel visible-light-induced Ag/BiOI, *Appl. Catal., B*, 2012, **111**(2), 271–279.

21 H. L. Lin, Y. J. Zhao, Y. J. Wang, J. Cao and S. F. Chen, Controllable in situ synthesis of Ag/BiOI and Ag/AgI/BiOI composites with adjustable visible light photocatalytic performances, *Mater. Lett.*, 2014, **132**(10), 141–144.

22 J. Cao, Y. J. Zhao, H. L. Lin, B. Y. Xu and S. F. Chen, Facile synthesis of novel Ag/AgI/BiOI composites with highly enhanced visible light photocatalytic performances, *J. Solid State Chem.*, 2013, **206**(10), 38–44.

23 T. T. Li, S. L. Luo and L. X. Yang, Three-dimensional hierarchical Ag/AgI/BiOI microspheres with high visible-light photocatalytic activity, *Mater. Lett.*, 2013, **109**(10), 247–252.

24 W. Qi, X. D. Shi, E. Q. Liu, J. C. Crittenden, X. J. Ma, Y. Zhang and Y. Q. Cong, Facile synthesis of AgI/BiOI-Bi₂O₃ multi-heterojunctions with high visible light activity for Cr(VI) reduction, *J. Hazard. Mater.*, 2016, **317**, 8–16.

25 H. Q. Li, Y. M. Cui and W. S. Hong, High photocatalytic performance of BiOI/Bi₂WO₆ toward toluene and reactive brilliant red, *Appl. Surf. Sci.*, 2013, **264**(1), 581–588.

26 Y. Q. Wang, X. F. Cheng, X. T. Meng, H. W. Feng, S. G. Yang and C. Sun, Preparation and characterization of Ag₃PO₄/BiOI heterostructure photocatalyst with highly visible-light-induced photocatalytic properties, *J. Alloys Compd.*, 2015, **632**, 445–449.

27 T. Yan, M. Sun, H. Y. Liu, T. T. Wu, X. J. Liu, Q. Yan, W. G. Xu and B. Du, Fabrication of hierarchical BiOI/Bi₂MoO₆ heterojunction for degradation of bisphenol A and dye under visible light irradiation, *J. Alloys Compd.*, 2015, **634**(1), 223–231.

28 H. Q. Li, Y. M. Cui, W. S. Hong and B. L. Xu, Enhanced photocatalytic activities of BiOI/ZnSn(OH)₆, composites towards the degradation of phenol and photocatalytic H₂ production, *Chem. Eng. J.*, 2013, **228**(14), 1110–1120.

29 J. Cao, B. Y. Xu, H. L. Lin, B. D. Luo and S. F. Chen, Chemical etching preparation of BiOI/BiOBr heterostructures with enhanced photocatalytic properties for organic dye removal, *Chem. Eng. J.*, 2012, **185–186**(1), 91–99.

30 K. K. Tiong and T. S. Shou, Anisotropic electrolyte electroreflectance study of rhenium-doped MoS₂, *J. Phys.: Condens. Matter*, 2000, **12**(23), 5043–5052.

31 H. Wan, L. Xu, W. Q. Huang, J. H. Zhou, C. N. He, X. F. Li, G. F. Huang, P. Peng and Z. G. Zhou, Band structure engineering of monolayer MoS₂: a charge compensated codoping strategy, *RSC Adv.*, 2015, **5**(11), 7944–7952.

32 Y. G. Li, Y. L. Li, C. M. Araujo, W. Luo and R. Ahuja, Single-layer MoS₂ as efficient photocatalyst, *Catal. Sci. Technol.*, 2013, **3**(9), 2214–2220.

33 W. Y. Gao, M. Q. Wang, C. X. Ran and L. Li, Facile one-pot synthesis of MoS₂ quantum dots-graphene-TiO₂ composites for highly enhanced photocatalytic properties, *Chem. Commun.*, 2015, **51**(9), 1709–1712.

34 X. W. Li, J. X. Xia, W. S. Zhu, J. Di, B. Wang, S. Yin, Z. G. Chen and H. M. Li, Facile synthesis of few-layered MoS₂ modified BiOI with enhanced visible-light photocatalytic activity, *Colloids Surf., A*, 2016, **511**, 1–7.

35 M. J. Islam, D. A. Reddy, N. S. Han, J. Choi, K. J. Song and T. K. Kim, An oxygen-vacancy rich 3D novel hierarchical MoS₂/BiOI/AgI ternary nanocomposite: Enhanced photocatalytic activity through photogenerated electron shuttling in a Z-scheme manner, *Phys. Chem. Chem. Phys.*, 2016, **18**(36), 24984–24993.

36 Y. Feng, L. Li, J. Li, J. Wang and L. Liu, Synthesis of mesoporous BiOBr 3D microspheres and their photodecomposition for toluene, *J. Hazard. Mater.*, 2011, **192**, 538–544.

37 X. Gao, X. Zhang, Y. Wang, S. Peng, B. Yue and C. Fan, Rapid synthesis of hierarchical BiOCl microspheres for efficient photocatalytic degradation of carbamazepine under simulated solar irradiation, *Chem. Eng. J.*, 2015, **263**, 419–426.

38 J. Henle, P. Simon, A. Frenzel, S. Scholz and S. Kaskel, Nanosized BiOX (X = Cl, Br, I) Particles Synthesized in Reverse Microemulsions, *Chem. Mater.*, 2007, **19**, 366–373.

39 S. Wu, H. Huang, M. Shang, C. Du, Y. Wu and W. Song, High visible light sensitive MoS₂ ultrathin nanosheets for photoelectrochemical biosensing, *Biosens. Bioelectron.*, 2017, **92**, 646–653.

40 S. Huang, J. Zhong, J. Li, J. Chen, Z. Xiang, M. Li and Q. Liao, Charge separation and photocatalytic properties of BiOI prepared by ionic liquid-assisted hydrothermal method, *Mater. Lett.*, 2016, **183**, 248–250.

41 S. M. Aghdam, M. Haghighi, S. Allahyari and L. Yosefi, Precipitation dispersion of various ratios of BiOI/BiOCl nanocomposite over g-C₃N₄ for promoted visible light nanophotocatalyst used in removal of acid orange 7 from water, *J. Photochem. Photobiol., A*, 2017, **338**, 201–212.

42 H. Wang, L. Ma, M. Gan and T. Zhou, Design and fabrication of macroporous polyaniline nanorods@graphene-like MoS₂, nanocomposite with high electrochemical performance for supercapacitors, *J. Alloys Compd.*, 2017, **699**, 176–182.

43 Z. Liu, X. X. Xu, J. Fang, X. M. Zhu, J. H. Chu and B. J. Li, Microemulsion synthesis, characterization of bismuth oxyiodine/titanium dioxide hybrid nanoparticles with outstanding photocatalytic performance under visible light irradiation, *Appl. Surf. Sci.*, 2012, **258**(8), 3771–3778.

44 A. C. Mera, Y. Moreno, D. Contreras, D. Escalona, M. F. Melendrez, R. V. Mangalaraja and H. D. Mansilla, Improvement of the BiOI photocatalytic activity optimizing the solvothermal synthesis, *Solid State Sci.*, 2017, **63**, 84–92.

45 Y. Xu and M. A. A. Schoonen, The absolute energy positions of conduction and valence bands of selected semiconducting minerals, *Am. Mineral.*, 2000, **85**, 543–556.